Developing New Detection Approaches for a Rubidium Vapor-based Atomic Magnetometer

A thesis submitted in partial fulfillment of the requirement
for the degree of Bachelor of Science with Honors in
Physics from the College of William and Mary in Virginia,

by

Owen C. Rollins

Advisor: Prof. Irina Novikova

Prof. S. Mordijck

Prof. L. Shaw

Williamsburg, Virginia
May 8 2026

Contents

Acknowledgments **iii**

List of Figures **v**

Abstract **v**

1 Introduction **1**

1.1 Overview of Magnetometry Techniques 1

1.2 Goals for this Work 2

2 Atomic Magnetometry Approach **3**

2.1 Atomic Absorption and Fluorescence 3

2.2 Electromagnetically Induced Transparency 4

2.3 The Zeeman Effect and Scalar Magnetometry 5

2.4 Polarization Selection Rules and Vector Magnetometry 7

2.4.1 Azimuthal Angle Detection 8

2.4.2 Longitudinal Angle Detection 9

3 Vector Magnetometer Configuration **11**

3.1 Laser and Electro-Optic Modulator 11

3.2 Vector Vortex Beam 12

3.3 Rubidium Cell and Helmholtz Coils 13

4 Camera and Image Processing **15**

4.1 Fourier Transform Low Pass Filter 16

4.2 Slicing Algorithm 17

4.3 Off-EIT Subtraction 19

4.4 EIT Profile Normalization 20

5 Angular Measurement Sensitivity **21**

5.1 Azimuthal Angle Measurement 21

5.2 Longitudinal Angle Measurement 24

5.2.1 EIT Variance with Angle 24

5.2.2 Signal Harmonic Analysis 26

5.2.3 Calibration Curve 27

6 Gradient Measurements **30**

6.1 Fluorescence Images 30

6.2 Magnetic Field Reconstruction 31

7 Conclusion **34**

References **35**

Acknowledgments

I would first like to thank Dr. Irina Novikova and Dr. Eugeniy Mikhailov for their tireless support and mentorship for the past three years, as well as Dr. Saskia Mordijck and Dr. Leah Shaw for serving on my thesis committee. My gratitude goes out to the entirety of the William & Mary Quantum Optics group, especially Nic DeStefano, Charris Gabaldon, and Rob Behary for their expert advice, as well as Will Torg and Kalea Wen for being excellent collaborators. I am grateful to William & Mary Charles Center for awarding me an Honors Fellowship to make this project possible. Lastly, I wish to thank my friends and family for always supporting me.

List of Figures

2.1 Two-level atom diagram. 3

2.2 Three-level atom diagram (left) and example EIT transmission peak (right). 5

2.3 Level diagram of ^{87}Rb D1 spectral line. 6

2.4 A magnetic field is applied to ^{87}Rb atoms, producing seven EIT peaks [7]. 7

2.5 Diagram of the two angles used to describe magnetic field direction. . 8

2.6 Variance of EIT brightness with ϕ, shown for all seven resonances [6]. 8

3.1 Experimental setup diagram. 11

3.2 Polarization profile of a radially polarized vortex beam. Arrows represent polarization direction. 12

3.3 Helmholtz coil setup with cell inside. 14

4.1 An example of a raw image of camera output. Here, interference is visible as a stripe pattern overlaid upon the beam. 15

4.2 Diagram of image filtering scheme. In this figure, the two images on the left are in image space and the two images on the right are in frequency space. 17

4.3 Illustration of what one-degree-width slices look like at each upscaling factor (top row); sliced brightness values against ϕ (bottom row) . . . 18

4.4 a_2 EIT brightness obtained by subtracting two images 19

5.1 EIT brightness at different resonances. Figure from [8] 22
5.2 EIT brightness as a function of ϕ for four different EIT peaks. 23
5.3 Results of ϕ measurement procedure for small (left) and large (right) angles. 23
5.4 EIT brightness images shown at a variety of different angles of θ. . . 24
5.5 EIT contrast as a function of ϕ, plotted for a variety of different angles of θ. 25
5.6 Harmonic analysis of EIT contrast curve at $\theta = 20°$. The shape of this curve is dominated by the A_1 term. 26
5.7 Harmonic analysis of EIT contrast curve at $\theta = 90°$. The shape of this curve relies on both the A_1 term and the A_2 term. 27
5.8 Calibration curve for measurement of θ derived from amplitude ratios. Each point is one degree apart. 28
5.9 In (a), the value of each of the three amplitudes as a function of θ. In (b), the calibration curve for measurement of θ. Each point is one degree apart. Taken from [8]. 29

6.1 Atomic fluorescence of rubidium atoms in the path of the laser, observed by a camera. 31
6.2 Fluorescence spectrum for a magnetic field configuration without strong gradients. 32
6.3 Fluorescence spectrum for a magnetic field configuration with strong gradients. 32
6.4 Example EIT spectra taken from figure 6.3. Both spectra represent one column from the fluorescence spectrum plot. 33

Abstract

Robust measurements of magnetic field can require measurement of vector field or magnetic field gradients, but many current approaches only perform scalar measurements. In this thesis, we present two new detection approaches for an atomic magnetometer that address these missing capabilities. The magnetometer uses Electromagnetically Induced Transparency (EIT) as a tool to investigate Zeeman-shifted atomic sublevels of ^{87}Rb. Equipping an EIT magnetometer with a radially polarized vector vortex beam enables fast vector measurement; with this approach, we demonstrate error less than a degree for the azimuthal angle of transverse fields. We also show a single-valued discrimination curve for the longitudinal angle of a general field and outline a corresponding measurement protocol for magnetic field direction. To image magnetic field gradients, measuring EIT via atomic fluorescence provides spatially-resolved information of magnetic field strength. Using this approach, we demonstrate sensitivity to longitudinal magnetic field gradients.

Chapter 1

Introduction

1.1 Overview of Magnetometry Techniques

Measuring magnetic fields is a problem that dates back thousands of years. However, recent innovations in other fields have turned up new and exciting applications for precise magnetometry, ranging from instrumentation on spacecraft to medical imaging [1, 2]. Over the years, various approaches to magnetometry have been developed, each with their own pros and cons. Hall-effect probes can be readily miniaturized, but lack the precision for the most sensitive applications. Fluxgate magnetometers are among the best classical devices, but still cannot compare in sensitivity to quantum sensors such as the superconducting quantum interference device (SQUID) or the spin-exchange relaxation-free (SERF) magnetometer [1, 3].

SQUIDs have emerged as the premier magnetometer for imaging contexts due to their high precision, but they have numerous drawbacks. Operation of these devices requires cryogenic infrastructure, thus limiting the detection proximity for a living subject. Furthermore, SQUIDs only operate well for weak magnetic fields, meaning their use for medical imagery is restricted to specialized rooms that shield off the external magnetic field. SQUIDs are also incapable of measuring the direction of magnetic fields [4].

Recently, atomic magnetometers such as SERF magnetometers have begun to approach sensitivity levels previously only attained by SQUIDs [4]. While atomic magnetometers have many advantages, such as independence from external calibration, even these SERF devices cannot measure magnetic field direction without heavy modification [5]. Furthermore, SERF magnetometers are also designed for use at very low fields. Previous work on an atomic magnetometer scheme known as an electromagnetically induced transparency (EIT) magnetometer has provided the best progress towards a precise vector sensor [6, 7]. The drawback of these devices is a requirement for active polarization rotation of laser light, usually requiring physically moving parts, and thus limiting the speed and reliability of the instrument.

1.2 Goals for this Work

In this thesis, we aim to establish the capability for vector magnetic field measurements using an atomic magnetometer with an eye towards future sensing applications. This device should be able to measure both angles of magnetic field and should operate without active polarization rotation, while preserving the desirable qualities of a precise atomic magnetometer. In the interest of broadening the information available through atomic magnetometry, we also explore a technique for measuring magnetic field gradients in the same system.

Chapter 2

Atomic Magnetometry Approach

2.1 Atomic Absorption and Fluorescence

Atoms can occupy certain stable energy levels given by the stable states of the atomic Hamiltonian. An example of two stable states, $|1\rangle$ and $|3\rangle$, is shown in figure 2.1. Here, the lower-energy state $|1\rangle$ is known as a ground state and the higher-energy state $|3\rangle$ is known as an excited state. When a photon with energy equal to the difference between two energy levels is incident upon an atom, the atom can absorb the photon; as a result, it will be enter the excited state. In this case, the light source is said to be *on resonance*. Referring to figure 2.1, an atom in state $|1\rangle$ can absorb a photon of energy $\hbar\omega_1$ and enter state $|3\rangle$. If a laser with frequency ω_l shines upon these atoms, some of the laser light will be absorbed when $\omega_l = \omega_1$. Sweeping ω_l produces an absorption signal. With the rubidium atoms used in this experiment, this absorption signal will be roughly 500 MHz wide.

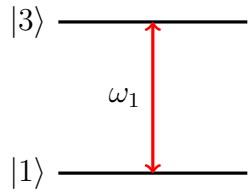

Figure 2.1: Two-level atom diagram.

Just as atoms in the ground state can absorb photons with energy $\hbar\omega_1$, atoms in the excited state $|3\rangle$ can *emit* photons of energy $\hbar\omega_1$ and return to the ground state $|1\rangle$. This process is known as fluorescence. Just as measuring absorption provides information about how many atoms are being excited from the ground state, measuring fluorescence provides information about how many atoms are decaying from the excited state.

2.2 Electromagnetically Induced Transparency

Real atoms are not as simple as the toy model shown in figure 2.1, and new energy levels bring additional effects, including electromagnetically induced transparency (EIT). EIT is an optical phenomenon that occurs when a three-level atom, such as the one shown in figure 2.2, interacts with a bichromatic, or two-frequency, laser field where both frequencies of light are on resonance. In this situation, the atom can enter a stable state called the dark state:

$$|D\rangle = \frac{\Omega_2 |1\rangle - \Omega_1 |2\rangle}{\sqrt{\Omega_1^2 + \Omega_2^2}} \tag{2.1}$$

where Ω_j is the Rabi frequency of the transition from $|j\rangle$ to the excited state $|3\rangle$. Here, it is crucial to note that $\langle 3|D\rangle = 0$, so the dark state is orthogonal to the excited state. For this reason, atoms in the dark state will not fluoresce (hence the name "dark state") and will not absorb light—even though they are interacting with laser fields at the atomic resonant frequencies.

As the dark state population is not excited by the laser, measuring laser transmission will produce a spike when the difference $\Delta\omega$ between the two laser frequencies—known as the *two-photon detuning*—matches the frequency difference between the two atomic ground states $\Delta\omega_{12}$. When measuring atomic fluorescence, atoms in the dark state will be invisible.

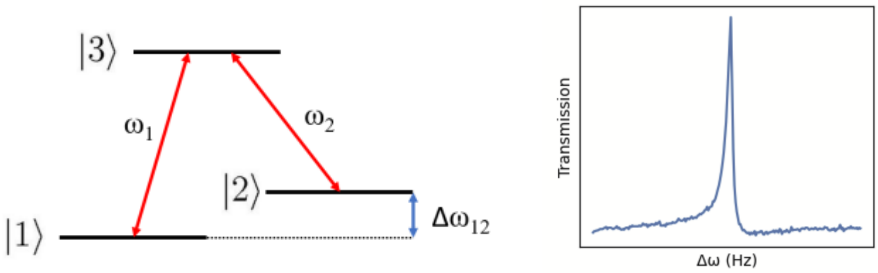

Figure 2.2: Three-level atom diagram (left) and example EIT transmission peak (right).

Since the dark state is a very stable, long-lived state, EIT produces a narrow resonance even in hot atoms [7], with linewidths on the order of a few kHz—five orders of magnitude narrower than the one-photon absorption resonance. Using EIT thus allows for precise measurement of atomic energy levels by measuring frequency.

2.3 The Zeeman Effect and Scalar Magnetometry

In this experiment, we use the D1 line of ^{87}Rb. The level diagram of this transition is shown in figure 2.3. The magnetic sublevels of the ground states $F = 1$ and $F = 2$ are degenerate in the absence of a magnetic field. When a magnetic field $\vec{B}$ is applied to the system, a phenomenon known as the Zeeman effect shifts the energy levels by

$$\Delta E_m = m\hbar\gamma B \tag{2.2}$$

where $\gamma = 7\text{Hz/nT}$ is a constant property of rubidium, $m = m_F$ is the azimuthal quantum number with quantization axis dictated by the magnetic field, and $B = |\vec{B}|$ is the scalar strength of the magnetic field. The quantum number m_F can take on the values $-F, -F+1, \ldots, F-1, F$: a total of $2F+1$ values. When $B = 0$, the Zeeman shift ΔE_m is zero, and these $2F+1$ sublevels are degenerate. But when magnetic field is applied, each previously degenerate state will have a different Zeeman shift based on its value of m_F. As a result, the $F = 1$ state will split 3-fold and the $F = 2$

state will split 5-fold, as seen in figure 2.3.

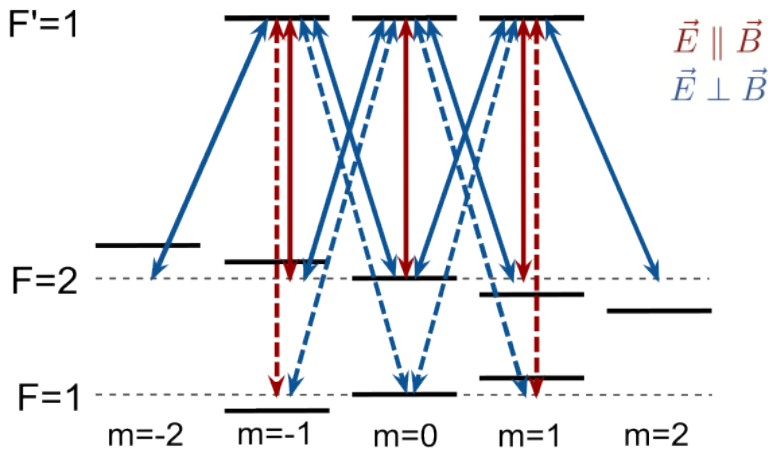

Figure 2.3: Level diagram of ^{87}Rb D1 spectral line.

In section 2.2 we discussed EIT in an atom with two ground states and a shared excited state. Now, we have an atom with far more than two ground states. For instance, a 3-level system could have ground states $|1\rangle = |F = 2, m = -2\rangle$ and $|2\rangle = |F = 1, m = -1\rangle$ with their shared excited state $|3\rangle = |F' = 1, m = -1\rangle$. Recall that EIT is achieved when the two-photon detuning Δw is equal to the difference between the ground states Δw_{12}, and note that $|1\rangle$ here has a Zeeman shift of $2m\hbar\gamma B$ and $|2\rangle$ has a Zeeman shift of $m\hbar\gamma B$. The EIT peak will thereby be shifted by $3m\hbar\gamma B$. On the contrary, another 3-level system is formed by $|1\rangle = |F = 2, m = 2\rangle$ and $|2\rangle = |F = 1, m = 1\rangle$ with their shared excited state $|3\rangle = |F' = 1, m = 1\rangle$. The EIT peak created by this 3-level system will have a total shift from the Zeeman effect equal to $-3m\hbar\gamma B$. It is possible to identify 3-level systems and their resulting EIT peaks at a total of seven different frequencies, equal to $a\hbar\gamma B$ for $a = -3, -2, -1, 0, 1, 2, 3$. We label these EIT peaks $a_{-3}, \ldots, a_3$. All seven EIT peaks are shown and labeled in figure 2.4. Note the constant spacing of $\hbar\gamma B$ between each peak.

As each EIT peak shifts linearly with the magnetic field, measuring the amplitude of the magnetic field B can be done by measuring the frequency at which each EIT

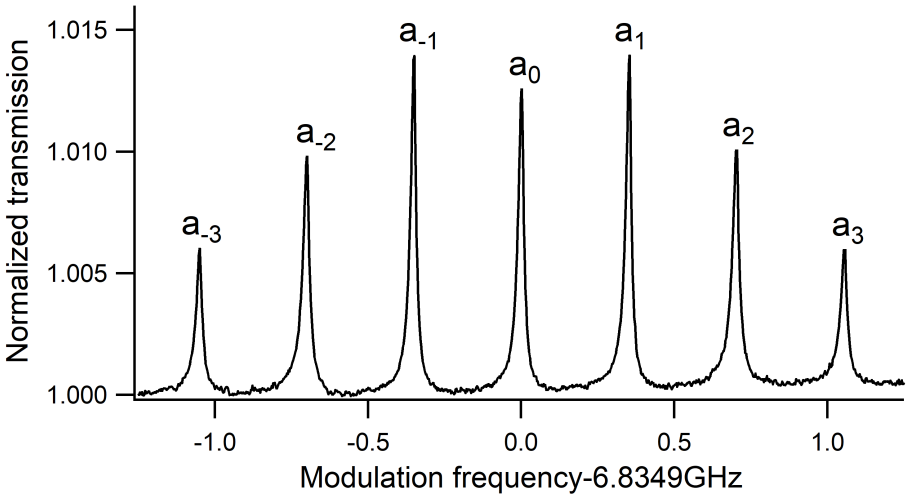

Figure 2.4: A magnetic field is applied to ^{87}Rb atoms, producing seven EIT peaks [7].

peak occurs and using equation 2.2 to solve for the magnetic field. We have previously used this approach to create a sensitive scalar magnetometer [7].

2.4 Polarization Selection Rules and Vector Magnetometry

Optical transitions in atoms are subject to a set of quantum selection rules. In particular, only transitions where $\Delta m = 0$ or $\Delta m = 1$ are permitted due to the conservation of angular momentum between the atom and the photon. Further rules on optical transitions relate to the polarization of laser light $\vec{E}$ relative to the external magnetic field $\vec{B}$. When $\vec{E} \parallel \vec{B}$, only transitions with $\Delta m = 0$ (shown in red in figure 2.3) are permitted. When $\vec{E} \perp \vec{B}$, only transitions with $\Delta m = \pm 1$ (shown in blue in figure 2.3) are permitted. At any intermediate polarization, both sets of transmissions are permitted at varying amplitudes.

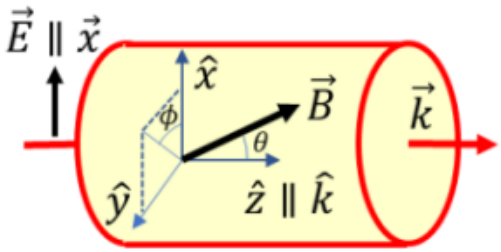

Figure 2.5: Diagram of the two angles used to describe magnetic field direction.

2.4.1 Azimuthal Angle Detection

The transition selection rules provide the backbone of the strategy used for vector magnetometry. We will reference three vectors: the polarization direction $\vec{E}$, the external magnetic field direction $\vec{B}$, and the laser wave vector $\vec{k}$, which points in the direction of laser propagation. We will also define two angles: the azimuthal angle ϕ, between $\vec{k} \times \vec{B}$ and $\vec{E}$, and the longitudinal angle θ, between $\vec{B}$ and $\vec{k}$ (see figure 2.5). The rubidium system has a clearly defined behavior when $\phi = 0°$ or $90°$, as well as when $\phi = 180°$ or $270°$, since an entire set of transitions becomes prohibited, so extreme amplitudes of EIT (i.e., maxima or minima) occur at $\phi = 0°$ and $90°$ (as well as $\phi = 180°$ and $270°$), as shown in figure 2.6.

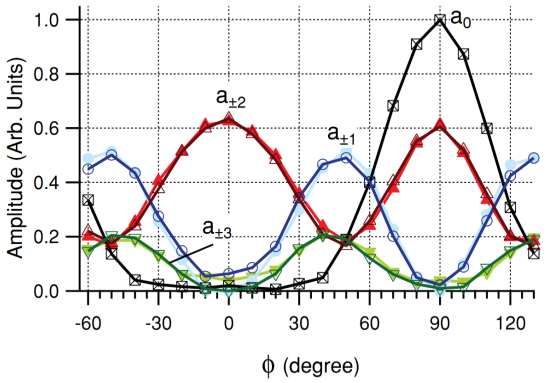

Figure 2.6: Variance of EIT brightness with ϕ, shown for all seven resonances [6].

Given this pattern, measuring ϕ requires finding the laser polarization $\vec{E}$ where

it is either parallel ($\phi = 0°$) or perpendicular ($\phi = 90°$) to the plane formed by $\vec{k}$ and $\vec{B}$ [7]. This can be done by altering polarization with a waveplate or other polarization rotator before the light enters the vapor cell. Any of the seven EIT resonances can be used for this purpose, as each have extrema at $\phi = 0°$ and 90°, but we use $a_{\pm 2}$ as it has high amplitude and retains sensitivity to scalar magnetic field strength, unlike a_0, which is not subject to the Zeeman shift. Previously, we attained ϕ angular sensitivity better than $1°/\sqrt{Hz}$ at all magnetic field angles and as good as $\sim 0.005°/\sqrt{Hz}$ at some angles using this method [7].

Despite its high sensitivity, this method may be difficult to put into practice for real-world sensing: making one measurement of ϕ requires rotating the laser polarization $\vec{E}$ repeatedly to search for either the parallel ($\phi = 0°$) or perpendicular ($\phi = 90°$) angles. Moving parts, such as those required for active polarization rotation, may be subject to additional wear and tear and thus be undesirable for use in a sensor. Additionally, this process takes time, and several magnetic field sensing applications deal with rapidly changing magnetic fields; in these cases this approach may fail to correctly identify either of the critical angles.

2.4.2 Longitudinal Angle Detection

Measuring the longitudinal angle θ is a little trickier, as there is no clear-cut best method like we used for ϕ. One strategy uses the fact that as θ changes, so does the effect of ϕ on EIT brightness. When $\theta = 90°$, both $\vec{E} \parallel \vec{B}$ and $\vec{E} \perp \vec{B}$ are possible, but when $\theta = 0°$, $\vec{E} \perp \vec{B}$ regardless of what $\vec{E}$ is. In this case, the blue transitions in figure 2.3 are entirely forbidden at all polarizations. As a result of this dependence, when ϕ is held constant but θ is varied, there is a resulting change in EIT amplitude.

We previously used this principle to measure the longitudinal angle [7]. This experiment, however, demonstrated that at around $\theta = 40°$ the intensity at the $a_{\pm 2}$

peak reaches a local minimum and the magnetometer as configured is insensitive to θ variation. Additionally, optimal ϕ sensitivity is attained at the configuration $\phi = 90°$ for some angles, but this configuration is entirely insensitive to θ.

Chapter 3

Vector Magnetometer Configuration

The central goal of this setup is to introduce a new method for vector magnetometry that resolves the issues with our previous approach, namely, the need for active polarization rotation and the need for multiple data points per measurement. Our strategy uses a type of laser beam with a spatial polarization distribution known as a vector vortex beam, which is introduced below. This chapter addresses key components of the magnetometer setup, as well as changes made to pursue our goals in vector measurement.

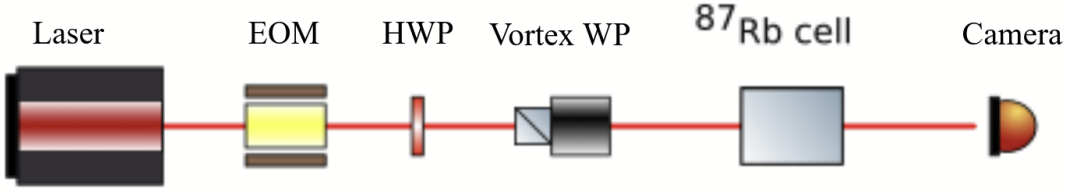

Figure 3.1: Experimental setup diagram.

3.1 Laser and Electro-Optic Modulator

The experimental setup for the magnetometer is shown in figure 3.1. The laser is locked to the $5S_{1/2}, F = 2 \rightarrow 5P_{1/2}, F' = 1$ transition of ^{87}Rb. As producing EIT

requires an atom interacting with two different frequencies, we pass our laser light through an electro-optic modulator (EOM). The EOM is driven at a frequency $\nu_{rf} \approx$ 6.835 GHz which can be controlled by an RF generator and outputs a beam with both the laser frequency and a sideband with the laser frequency plus ν_{rf}. That is, the two-photon detuning $\Delta\omega$ is set at ν_{rf} and controlled with the RF generator.

3.2 Vector Vortex Beam

To gain information about the EIT brightness at all values of light polarization, we use a vector vortex beam. In a vector vortex beam, the polarization of the light varies spatially over the profile of the beam, as shown in figure 3.2. Note that the center of the beam is dark as the various different polarizations overlap and destructively interfere.

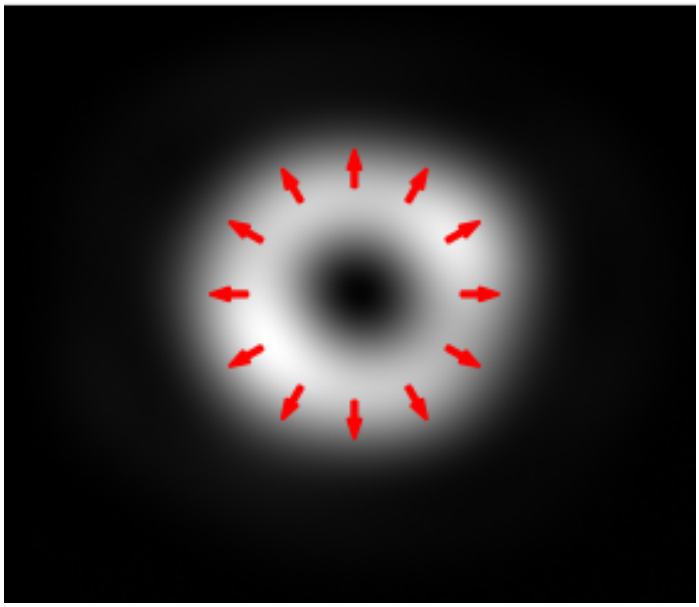

Figure 3.2: Polarization profile of a radially polarized vortex beam. Arrows represent polarization direction.

The vortex beam allows simultaneous investigation of every polarization angle at

the same time. Without the vortex beam, comparing $\phi = 0°$ and $90°$ meant taking one measurement, rotating a waveplate to change the laser polarization $\vec{E}$, and then taking a second measurement. With the vortex beam, one measurement will be in the form of an image, and comparing two different locations on the image can give the same information as the two measurements from before with no moving parts and no wait time. For this reason, we believe vector measurement with a vector vortex beam is a promising technique that could lend itself well to future applications.

It is worth noting that the vortex waveplate used in this experiment is designed for light with wavelength 780nm, whereas the laser in use has wavelength 795nm. We have found some evidence that the polarization distribution is not perfectly radial, and future work on this project will look to account for this fact.

3.3 Rubidium Cell and Helmholtz Coils

The rubidium cell used in this experiment contains ^{87}Rb vapor as well as 5 Torr of Ne buffer gas and measures 2.5 cm long. The cell is stabilized at 60° C and braced by a metal heatsink to concentrate condensed rubidium vapor away from the beam path.

The cell is placed inside a 3-dimensional Helmholtz coil setup. By driving current to each of the three pairs of coils, we can produce a magnetic field with arbitrary magnitude and direction over the cell for testing purposes. The cell-coil system is then covered by three layers of mu metal magnetic shielding to block out external magnetic fields for maximum control of the magnetic field in the cell. For this phase of the project, we make the assumption that the magnetic field is uniform inside the cell.

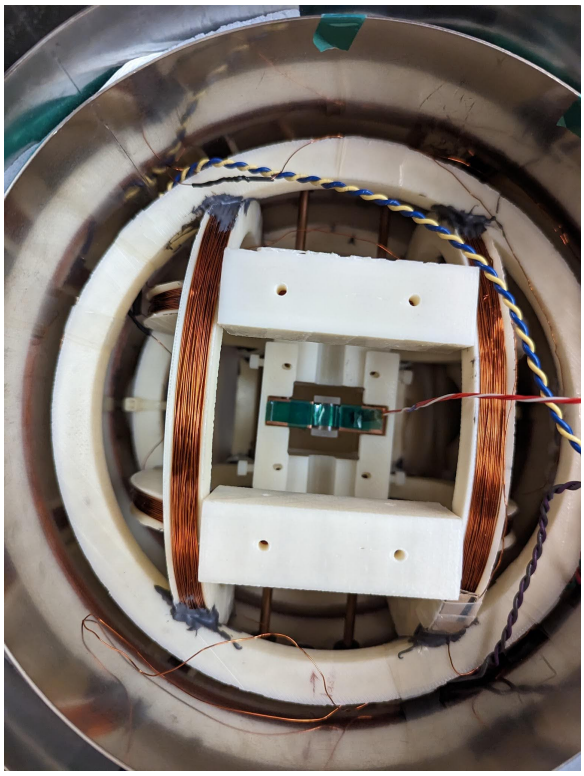

Figure 3.3: Helmholtz coil setup with cell inside.

Chapter 4

Camera and Image Processing

We have passed a spatially varying polarization distribution through our rubidium cell and wish to find the brightness as a function of polarization. Each image output image is 1280 by 1024—about 1.3 million individual pixel brightness values—but must be mapped to the range of polarization from 0° to 360°.

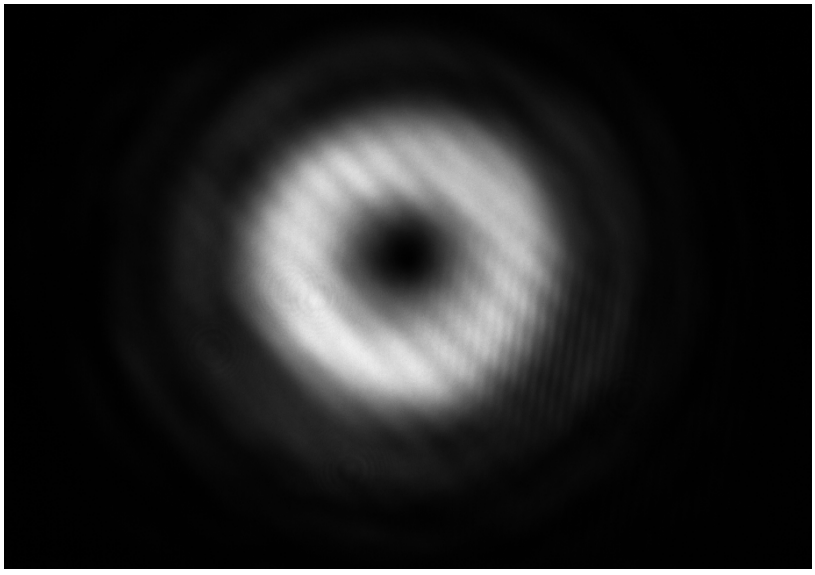

Figure 4.1: An example of a raw image of camera output. Here, interference is visible as a stripe pattern overlaid upon the beam.

Furthermore, every optical component in the system can introduce beam diffraction, distortion, or interference, which are not important to a photodetector but show

up readily on a camera. Indeed, a careful look at figure 4.1 reveals multiple different frequencies of interference fringes visible by eye. These fringes should be removed before any further processing. As a result, converting data from image form to a more easily comprehensible form is a nontrivial task.

4.1 Fourier Transform Low Pass Filter

As the interference patterns from optical components in the system do not carry any physical information about the dependence of brightness on polarization, we wish to remove as many of these patterns as possible during our data processing. Critically, we know that the EIT signal occupies a fixed range of spatial frequencies. As mentioned in section 2.4.1, the EIT signal can only have maxima at at most two critical angles, $\phi = 0°$ and $90°$, plus the corresponding angles $\phi = 180°$ and $270°$ for a total of four points across the vortex beam profile. Meanwhile, experimental noise in the form of interference fringes occupies the higher spatial frequencies. Observe this effect in figure 4.1, where the most easily visible frequency of interference fringes has at least ten bright and dark stripes. While interference noise *can* exist in frequencies similar to those of the signal, its spatial frequency can also be altered by slightly manually moving the optical components in the system, as the slit spacing between fringes is dependent on the angle at which light hits it. Therefore, our strategy for removing the experimental noise caused by interference is twofold: first, move all the interference fringes into the high frequency range; then, filter out the signals at a high spatial frequency.

To identify the spatial frequencies present in the image, we use a two-dimensional Fourier transform. In the two-dimensional Fourier domain, basis elements are sinusoids with the form $e^{2\pi i(ux+vy)}$ for integers u, v, where the overall frequency goes with $\sqrt{u^2+v^2}$. Therefore, placing a low pass filter on an image involves limiting the am-

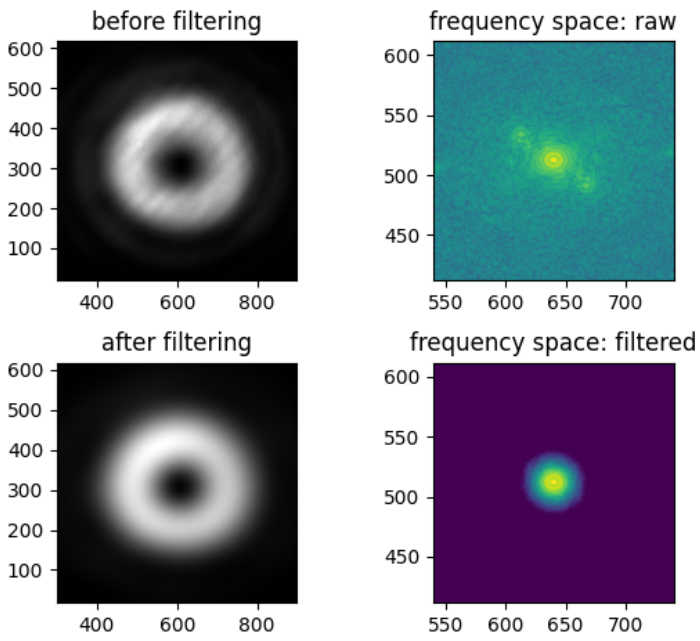

Figure 4.2: Diagram of image filtering scheme. In this figure, the two images on the left are in image space and the two images on the right are in frequency space.

plitudes of Fourier components with high $\sqrt{u^2+v^2}$, representing a circular mask in frequency space. This circular mask is shown in the lower right corner of figure 4.2, and the results of the filter are visible in the lower left corner. It is possible to tell by eye that the filter has removed much of the interference fringe noise.

4.2 Slicing Algorithm

To extract the ϕ-dependence of EIT contrast we overlay the polar coordinate grid over the image and integrate along one-degree slices of the angle ϕ to produce an average brightness value. Recall from section 2.4.1 that the polar angle corresponds with the polarization angle inflicted by the vortex waveplate, so ϕ truly does represent the angle of the field. The center of the coordinate grid is the center of mass of the image, ignoring low brightness pixels.

When cutting the image into slices, especially slices as narrow as one degree, com-

putational artifacts can arise from the uneven distribution of ϕ values across pixels. This results in a different number of pixels for each slice, introducing computational noise to brightness traces. To solve this problem, we expand our image by splitting each pixel n times in both the x and y directions; n is henceforth referred to as the upscaling factor. After upscaling, each pixel is split into n^2 identical copies of itself. Slices on this upscaled image are more regular in shape, as shown in the top row of figure 4.3.

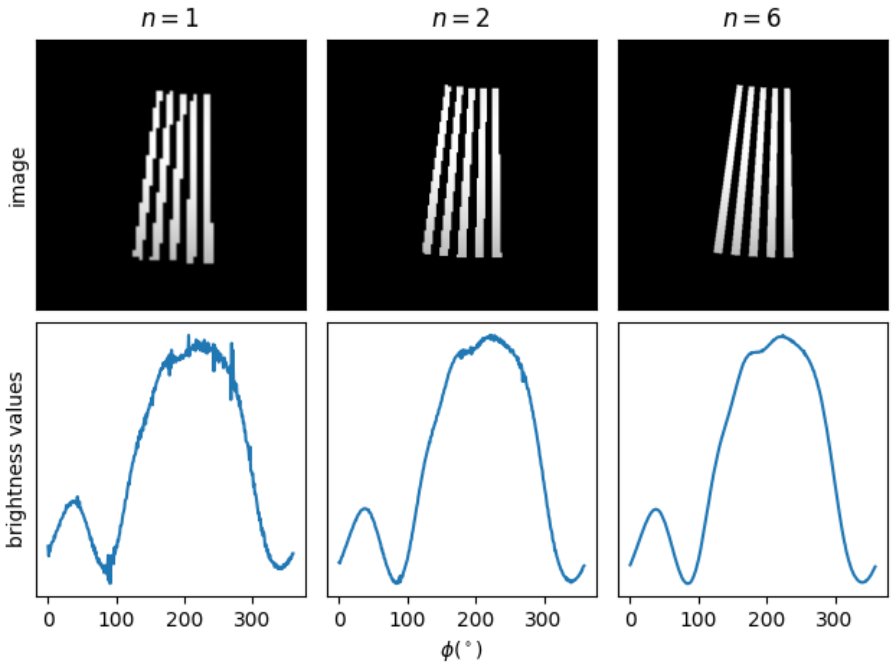

Figure 4.3: Illustration of what one-degree-width slices look like at each upscaling factor (top row); sliced brightness values against ϕ (bottom row)

Figure 4.3 demonstrates the effect of upscaling the image. The bottom half of the figure shows the result of the slicing algorithm at various different upscale factors. Overall, the shape of the slices becomes more regular, and noise in the signal accordingly goes down. This is an appreciable noise reduction brought about only by considering computational effects—no physical changes are involved by refining

the algorithm in this way. For further results, we set $n = 6$. While increasing the upscaling factor does can further smooth computational irregularities, it comes at the cost of lengthening data processing time quadratically with n.

4.3 Off-EIT Subtraction

EIT is not the only polarization-dependent phenomenon that affects laser transmission [7]. To measure the brightness of just the EIT contribution we take the difference of two measurements: one taken on the two-photon resonance, and one with the rf laser frequency tuned off the two-photon resonance. These two images can then be subtracted to isolate the effect of the brightness due only to EIT. Figure 4.4 shows the EIT brightness obtained by this subtraction for the a_2 EIT peak. Observe that there are EIT maxima, seen as bright spots, at each of the four critical angles described in section 2.4.1.

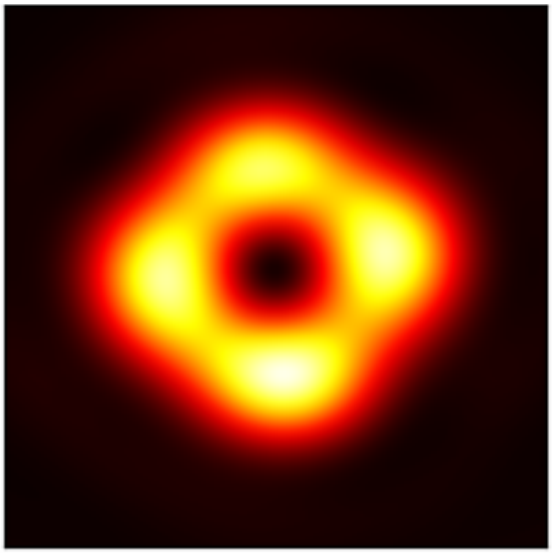

Figure 4.4: a_2 EIT brightness obtained by subtracting two images

4.4 EIT Profile Normalization

We define EIT contrast is defined as

$$contrast = \frac{EIT\ brightness}{background\ brightness} \tag{4.1}$$

The procedure for measuring EIT contrast is the same whether detection is done with a single-pixel photodetector or a camera, and involves the EIT brightness quantity discussed above. Every contrast curve is therefore the result of three images: a background image, an off-EIT image, and an on-EIT image. During magnetometer operation, the background image can be taken before any measurements and used to normalize all subsequent images. As a result, only two images are necessary to produce a contrast curve, whereas previous approaches required a measurement for each point along the curve. This advance is due to the information density provided by the vortex beam, and the precision capability of the camera detection scheme.

This contrast formula can be combined with the described filtering, slicing, and background subtracting processes to achieve, as desired, the dependence of EIT brightness on ϕ.

Chapter 5

Angular Measurement Sensitivity

5.1 Azimuthal Angle Measurement

As discussed in section 2.4.1, the EIT signal has extrema at four critical angles ($\phi = 0°,\ 90°,\ 180°,\ 270°$) for all seven EIT peaks. Previous work observed this phenomenon by taking multiple measurements at different polarizations, but we observe the same effect with only a pair of measurements (on-EIT and off-EIT) for each EIT peak. The image results are shown in figure 5.1 and the sliced brightness profiles are shown in figure 5.2. The a_0 and $a_{\pm 2}$ peaks are the brightest, but the a_0 peak is not sensitive to the magnitude of the magnetic field, so to preserve the scalar capability of the magnetometer we will use the a_2 peak for our measurements.

As the angle of the magnetic field changes with respect to the laser polarization, these extrema will shift along the ϕ axis and the pattern in figure 5.1 will appear to rotate. Since the polarization distribution present in the vortex beam is known, ϕ can be measured by finding the values of $\vec{E}$ at which ϕ reaches its extrema. Therefore, changes in the azimuthal angle of $\vec{B}$ can be detected via changes in the maximum and minimum values of EIT contrast. A notable limitation of this process is that it is not possible to distinguish between $\phi = 0°$ and $\phi = 180°$ in the current configuration.

The procedure for measuring the precision of this method is as follows. First,

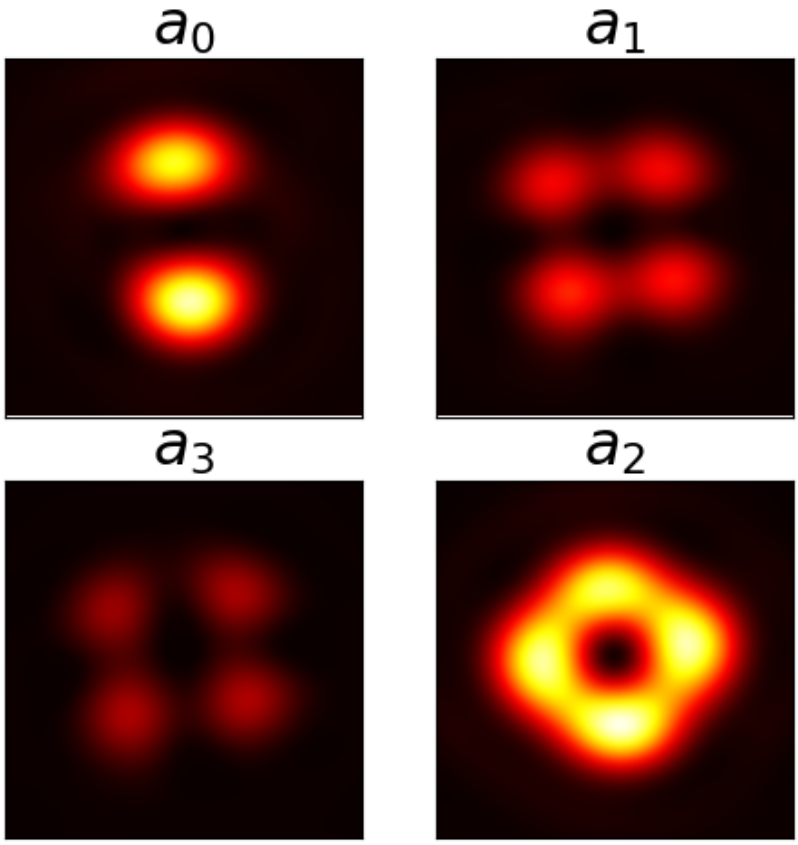

Figure 5.1: EIT brightness at different resonances. Figure from [8]

set the magnetic field in the cell to a reference ϕ angle. Next, set a range of test magnetic fields at differing ϕ angles and record EIT contrast images at each angle. After processing these data, computationally evaluate the derivative of these signals and calculate their zero crossings to establish the positions of EIT extrema. Lastly, compare the extrema positions at the test angle to the extrema positions at the reference angle. At transverse magnetic field ($\theta = 90°$), this results in eight extrema—the four maxima and four minima (see figure 5.5). Measuring ϕ therefore involves averaging the shift of each of these eight values; the standard deviation gives the error bar.

To test the accuracy of this measurement process, I produced a transverse mag-

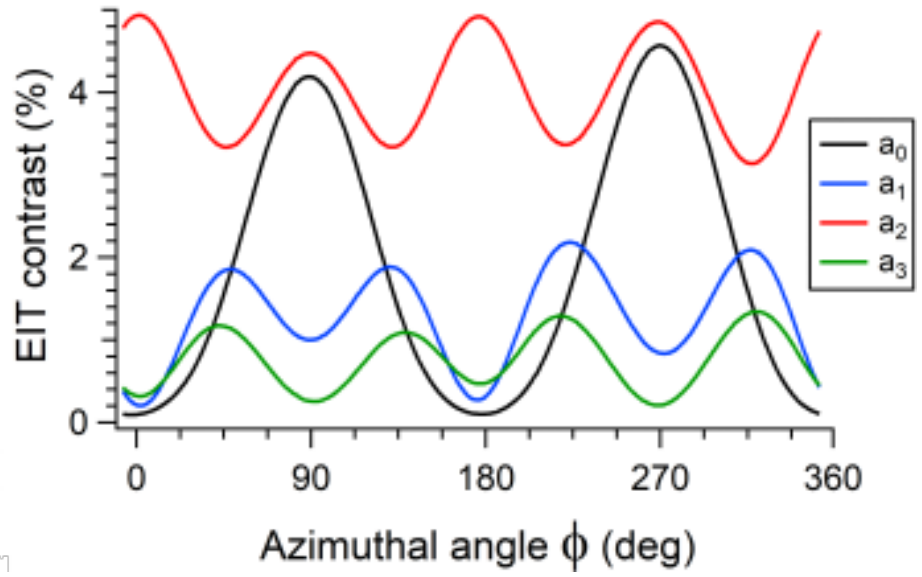

Figure 5.2: EIT brightness as a function of ϕ for four different EIT peaks.

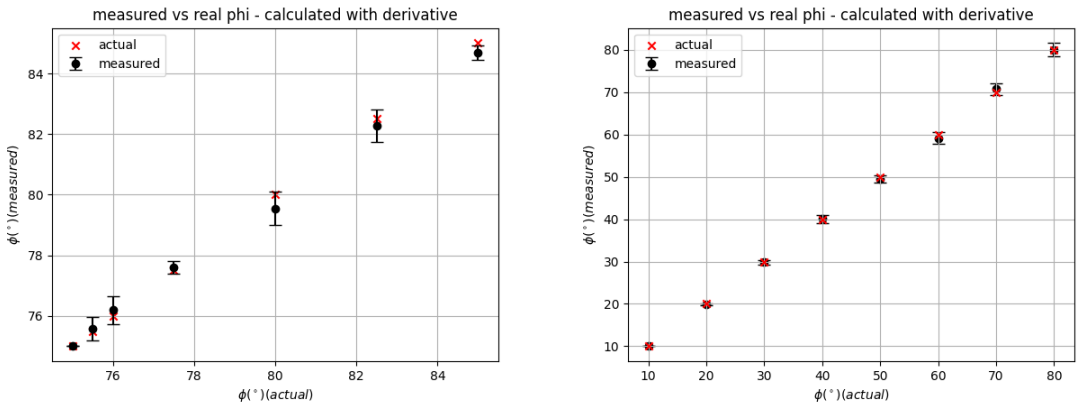

Figure 5.3: Results of ϕ measurement procedure for small (left) and large (right) angles.

netic field and changed ϕ by fixed steps to compare the measured ϕ to the true ϕ. The results are shown in figure 5.3. Overall, the measured ϕ follows the true value of ϕ fairly well. The root mean square error of these measurements is less than one degree, although at larger angle deviations the error bars grow, as seen on the right in figure 5.3. This is due to polarization imperfections in the vortex beam.

5.2 Longitudinal Angle Measurement

When measuring the longitudinal angle of magnetic field, recall that there is no analog to the critical angles used above for the azimuthal angle. Nonetheless, θ does affect the EIT brightness, as seen in figure 5.4. One can easily describe this dependence qualitatively—a shift from four maxima, to two, to a constant-brightness ring. The topic of this section will be an approach to quantifying this dependence.

5.2.1 EIT Variance with Angle

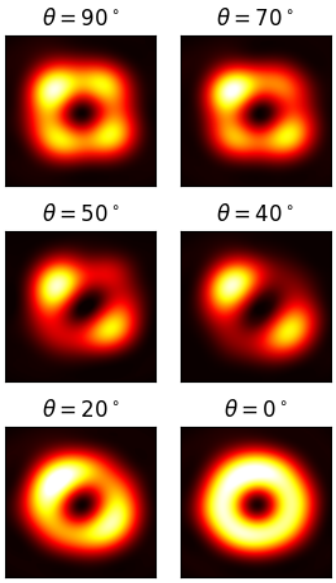

Figure 5.4: EIT brightness images shown at a variety of different angles of θ.

EIT contrast from various angles of θ is plotted in figure 5.5. At large θ (i.e., close

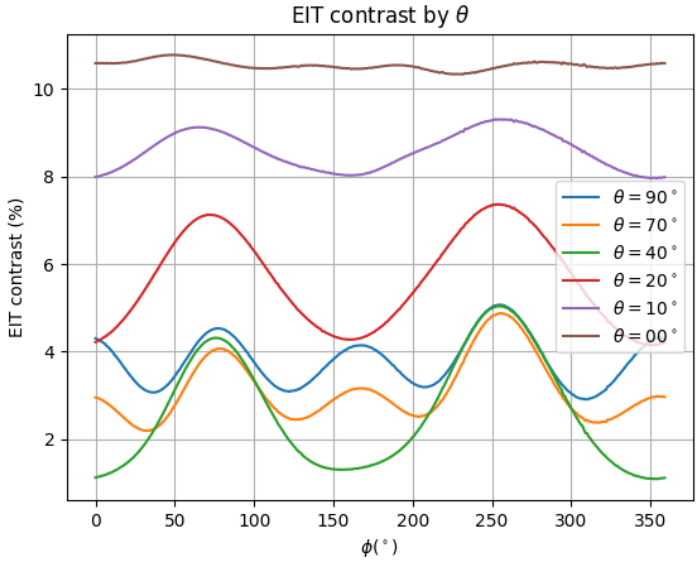

Figure 5.5: EIT contrast as a function of ϕ, plotted for a variety of different angles of θ.

to 90°), there are four angles of the azimuthal angle ϕ that produce a maximum value for EIT contrast: two where $\vec{E} \parallel \vec{B}$ and two where $\vec{E} \perp \vec{B}$. However, these pathways can destructively interfere with each other, and when $\theta < 90°$, there is no ϕ such that contribution of the $\vec{E} \perp \vec{B}$ disappears entirely. Indeed, figure 5.5 shows that the $\phi = 0°$ maximum disappears as θ decreases, and for small θ there are just two ϕ that give EIT maxima: $\phi = 90°$ and $\phi = 270°$. Lastly, as θ goes to zero, the configuration of the magnetometeter becomes symmetric to polarization rotation. Thus, ϕ loses meaning, and the EIT contrast curve approaches a straight line.

Figure 5.5 demonstrates that EIT contrast has a pronounced dependence on θ, suggesting this apparatus has a promising capability for measuring this angle. However, this task is significantly different from measuring the azimuthal angle ϕ. For one thing, the vortex beam enables investigating the full range of ϕ values, but no such capability for θ exists due to the geometry of the experiment. Additionally, there are two azimuthal angles—the perpendicular and parallel configurations—that always re-

sult in extreme values of EIT contrast, facilitating objective measurement. However, with no analogous feature of the system for the longitudinal angle, measurement of θ must rely on a calibration done in advance. Nonetheless, the EIT contrast pattern demonstrates that our system is responsive to θ and thus capable of its measurement.

5.2.2 Signal Harmonic Analysis

As discussed above, EIT contrast curves have three shapes: a constant value, periodic with two maxima across 360°, and periodic with four maxima across 360°. We quantify this idea by taking three terms from the Fourier expansion of the EIT contrast signal: constant, 180° period, and 90° period. I will henceforth refer to A_0 as the amplitude of the constant term, A_1 as the amplitude of the term with 180° period, and A_2 as the amplitude of the term with 90° period. Expressing each EIT contrast curve as a linear combination of these three basis functions yields values for $A_{0,1,2}$ that can be used as an identifier for θ.

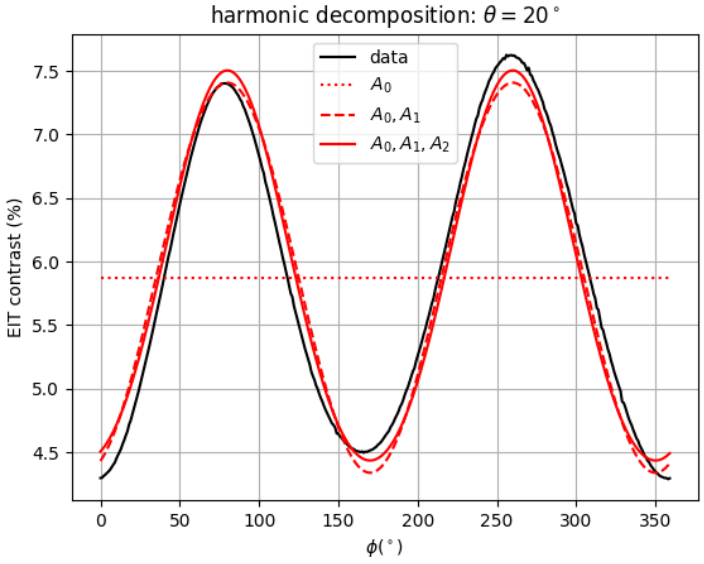

Figure 5.6: Harmonic analysis of EIT contrast curve at $\theta = 20°$. The shape of this curve is dominated by the A_1 term.

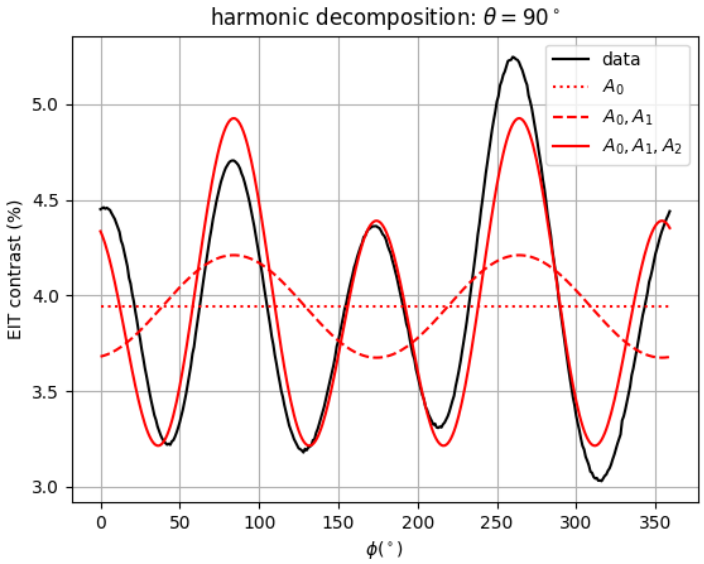

Figure 5.7: Harmonic analysis of EIT contrast curve at $\theta = 90°$. The shape of this curve relies on both the A_1 term and the A_2 term.

Two examples of this decomposition are seen in figures 5.6 and 5.7. In each, the dotted line represents the constant offset term corresponding to A_0, the dashed line represents the first harmonic corresponding to A_1, and the solid red line shows the final fit with both harmonics plotted.

5.2.3 Calibration Curve

To measure θ, we plot the quantities A_1 and A_2 against each other to produce a calibration curve. During measurement, one would measure these amplitudes and consult the calibration curve to find out the value of θ.

Our initial attempts at producing this curve centered around measuring ratios of amplitudes—that is, plotting A_1/A_0 and A_2/A_0 instead of directly comparing the amplitudes. The curve produced by this method is shown in figure 5.8. This approach was intended to increase resistance to power-dependent drifts and other experimental fluctuations. On the other hand, figure 5.9a shows that the largest experimental error

bars are on A_0. As a result, involving another parameter greatly increased the error bars on the calibration curve.

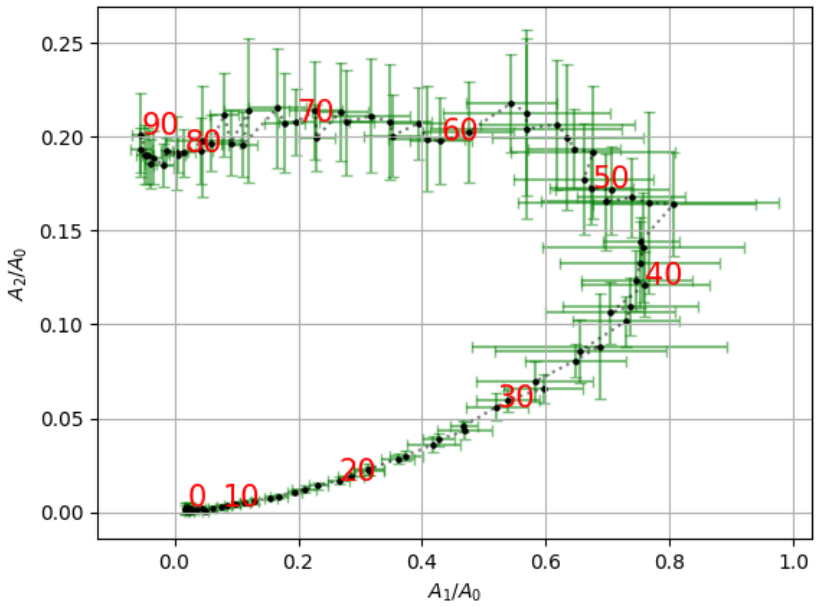

Figure 5.8: Calibration curve for measurement of θ derived from amplitude ratios. Each point is one degree apart.

Instead, choosing to use only A_1 and A_2 produced the curve shown in figure 5.9b, with much smaller error bars.

A major advantage of this approach is that the function is single valued; that is, providing values of the two amplitudes A_1 and A_2 will uniquely identify θ. In other words, the calibration curve does not cross itself in the two-dimensional parameter space defined by A_1 and A_2. This is especially noteworthy because under previous strategies, the magnetometer had blind spots at intermediate θ angles, especially between 40° and 50°.

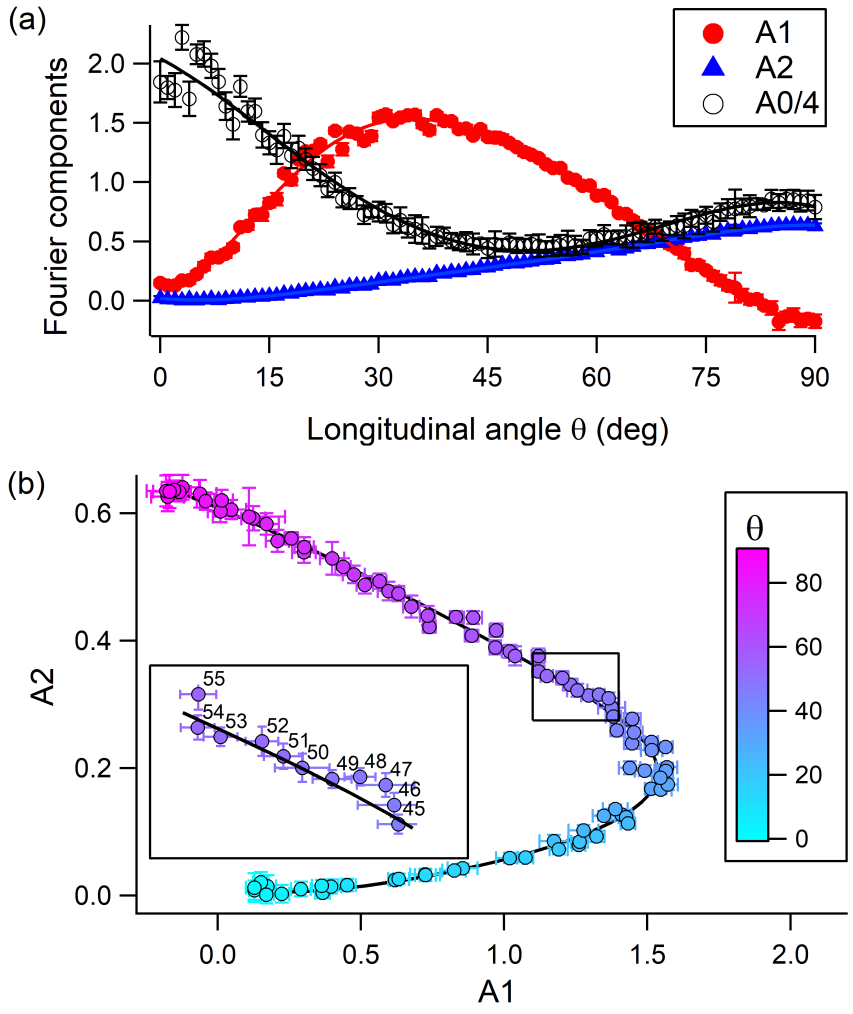

Figure 5.9: In (a), the value of each of the three amplitudes as a function of θ. In (b), the calibration curve for measurement of θ. Each point is one degree apart. Taken from [8].

Chapter 6

Gradient Measurements

We now pivot to a different measurement scheme in the hopes of detecting longitudinal gradients along the path of the laser beam. Any detection system similar to the one shown in figure 3.1 with a single detector at the end of the beam path, is not capable of capturing longitudinal B field variations as the beam travels the entire length of the cell and thus measures the averaged field over the path. Instead, we measure fluorescence of excited atoms in the beam path by directly photographing the rubidium vapor cell. As noted in section 2.1, atoms in the dark state do not fluoresce, so the beam becomes less bright in places where atoms are in an EIT resonance. Imaging fluorescence provides the additional information of observing specific parts of the cell enter the dark state.

6.1 Fluorescence Images

Positioning a camera above the vapor cell and turning on the laser gives photos of atomic fluorescence such as figure 6.1. It is worth noting that when atoms fluoresce, they do so in a random direction (i.e., not necessarily towards the camera), so the camera exposure time for figure 6.1 is about one hundred times longer than that used for figure 4.1.

Note also that the beam appears significantly brighter on the right side of the

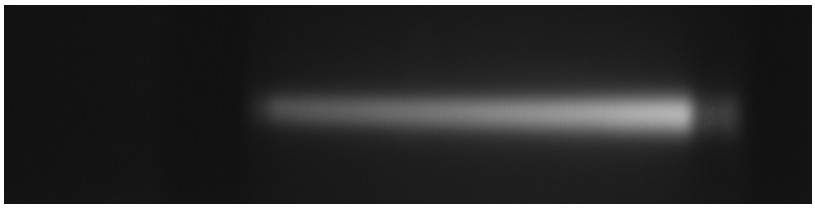

Figure 6.1: Atomic fluorescence of rubidium atoms in the path of the laser, observed by a camera.

image than the left. This is due to absorption by the atoms across the path of the beam. When the atoms are in the dark state, they do not fluoresce. As a result, the beam will become less bright in the locations where atoms are in an EIT resonance.

6.2 Magnetic Field Reconstruction

Measurements of magnetic field can be made by observing the atomic fluorescence at different values of two-photon detuning, similar to the process described in section 2.2. Then, a single image constitutes one measurement at that frequency. Sweeping the frequency and plotting the longitudinal brightness of each fluorescence image against frequency yields a fluorescence spectrum where EIT peaks show as negative brightnesses.

Figure 6.2 shows an example of a squid plot for the case without a magnetic field gradient. Seven dark lines, representing EIT peaks a_{-3} through a_3, are visible, and do not change in detuning (y-axis) by longitudinal position in the cell (x-axis).

Figure 6.3 shows an example of a squid plot for the case with a strong magnetic field gradient. Observe that the darker areas of the plot, signaling reduced fluorescence and thus EIT, occur at different detunings with z, the spatial position across the cell.

Each vertical slice of the squid plots shown here represents a full EIT spectrum only for the atoms at a specific position in the cell. These spectra can be retrieved, as shown in figure 6.3, and used to measure magnetic field. Here, the magnetic field

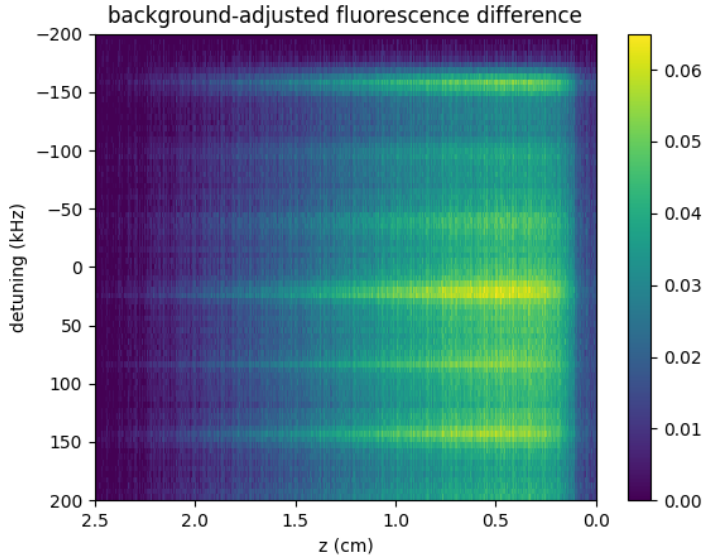

Figure 6.2: Fluorescence spectrum for a magnetic field configuration without strong gradients.

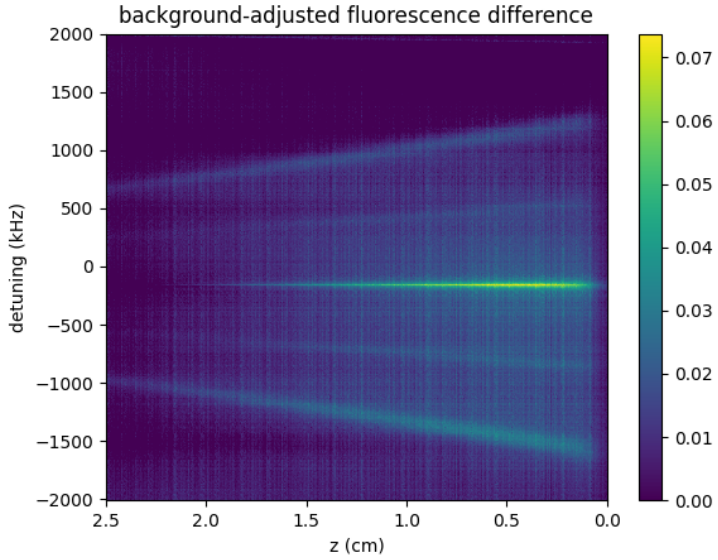

Figure 6.3: Fluorescence spectrum for a magnetic field configuration with strong gradients.

is stronger at column 1000, resulting in greater separation of peaks than at column 500. This effect is shown in figure 6.4, where both EIT spectra exhibit a_0 peaks at

the same frequency, but $a_{\pm 2}$ peaks at different frequencies.

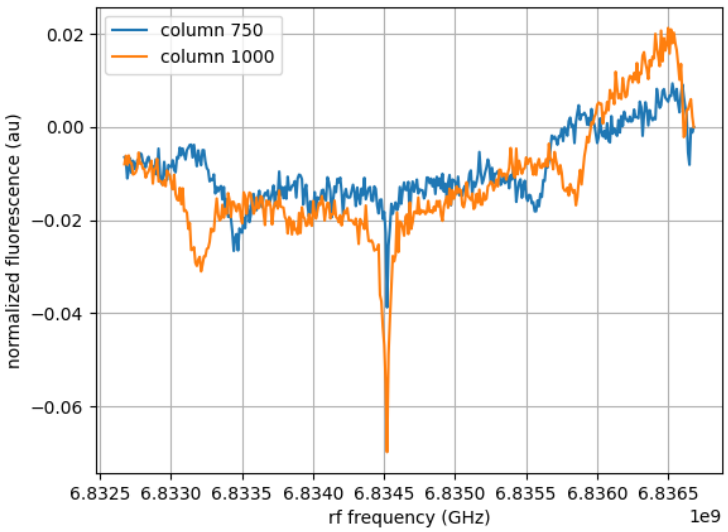

Figure 6.4: Example EIT spectra taken from figure 6.3. Both spectra represent one column from the fluorescence spectrum plot.

There is a great deal of noise in the measurement results shown here. This can be attributed in part to the slow measurement procedure, allowing time for systematic fluctuations between points. Furthermore, ensuring the camera is perfectly focused will help narrow the EIT peaks on the fluorescence spectrum by reducing blurriness of images. While the error is too large to be used for commercial measurements, the appearance of the squid plot shapes suggests that this method is sensitive to magnetic field gradients and could produce a more reliable measurement. Considerable work remains in optimizing and refining this technique.

Chapter 7

Conclusion

The scalar sensitivity of atomic magnetometers has been thoroughly investigated using a bevy of different approaches, but atomic magnetometers provide information about other qualities of magnetic field, too. This experiment suggests that, by pairing vortex beams with familiar EIT magnetometry techniques, a fast, accurate vector magnetometer can be realized with sub-degree accuracy on the azimuthal angle and a single-valued parametrization for the longitudinal angle. This approach avoids the need for active polarization rotation, requires just two data points per measurement, and is not subject to blind spots at some angles, making it well-suited for use in sensors. Future work will work to lessen reliance on an experimentally-derived calibration curve. In the more distant future, vector EIT magnetometers may leverage other patterns of spatial light or other experiment geometries entirely to increase their precision. This work also suggests that an atomic magnetometer setup can even detect magnetic field gradients in the direction of beam propagation. Increasing sensitivity in this device will require careful optimization of experimental parameters such as vapor temperature and camera focusing.

References

[1] C. Cochrane et al. "Vectorized magnetometer for space applications using electrical readout of atomic scale defects in silicon carbide". In: *Scientific Reports* 6 (2016). DOI: 10.1038/srep37077.

[2] Wei Xiao et al. "A movable unshielded magnetocardiography system". In: *Science Advances* 9.13 (2023), eadg1746.

[3] Anne Fabricant, Irina Novikova, and Georg Bison. "How to build a magnetometer with thermal atomic vapor: a tutorial". In: *New Journal of Physics* 25.2 (Feb. 2023), p. 025001. ISSN: 1367-2630. DOI: 10.1088/1367-2630/acb840. URL: http://dx.doi.org/10.1088/1367-2630/acb840.

[4] Dmitry Budker and Michael Romalis. "Optical magnetometry". In: *Nature Physics* 3.4 (Apr. 2007), pp. 227–234. ISSN: 1745-2481. DOI: 10.1038/nphys566. URL: https://doi.org/10.1038/nphys566.

[5] Aram Papoyan et al. "Magnetic-field-compensation optical vector magnetometer". In: *Appl. Opt.* 55.4 (Feb. 2016), pp. 892–895. DOI: 10.1364/AO.55.000892. URL: https://opg.optica.org/ao/abstract.cfm?URI=ao-55-4-892.

[6] Kevin Cox et al. "Measurements of the magnetic field vector using multiple electromagnetically induced transparency resonances in Rb vapor". In: *Phys. Rev. A* 83 (1 Jan. 2011), p. 015801. DOI: 10.1103/PhysRevA.83.015801. URL: https://link.aps.org/doi/10.1103/PhysRevA.83.015801.

[7] Mario González Maldonado et al. "Sensitivity of a vector atomic magnetometer based on electromagnetically induced transparency". In: *Optics Express* 32 (June 2024), pp. 25062–25073. DOI: 10.1364/OE.529276.

[8] Owen Rollins, Eugeniy E. Mikhailov, and Irina Novikova. "Magnetic field direction detection using electromagnetically induced transparency with a vector vortex beam". In: *Opt. Lett.* 51.4 (Feb. 2026), pp. 961–964. DOI: 10.1364/OL.585801. URL: https://opg.optica.org/ol/abstract.cfm?URI=ol-51-4-961.